

ARTICLE

Received 16 Nov 2012 | Accepted 21 Jan 2013 | Published 19 Feb 2013

DOI: 10.1038/ncomms2528

# Observation of longitudinal and transverse self-injections in laser-plasma accelerators

S. Corde<sup>1,\*</sup>, C. Thaury<sup>1,\*</sup>, A. Lifschitz<sup>1</sup>, G. Lambert<sup>1</sup>, K. Ta Phuoc<sup>1</sup>, X. Davoine<sup>2</sup>, R. Lehe<sup>1</sup>, D. Douillet<sup>1</sup>, A. Rousse<sup>1</sup> & V. Malka<sup>1</sup>

Laser-plasma accelerators can produce high-quality electron beams, up to giga electronvolts in energy, from a centimetre scale device. The properties of the electron beams and the accelerator stability are largely determined by the injection stage of electrons into the accelerator. The simplest mechanism of injection is self-injection, in which the wakefield is strong enough to trap cold plasma electrons into the laser wake. The main drawback of this method is its lack of shot-to-shot stability. Here we present experimental and numerical results that demonstrate the existence of two different self-injection mechanisms. Transverse self-injection is shown to lead to low stability and poor-quality electron beams, because of a strong dependence on the intensity profile of the laser pulse. In contrast, longitudinal injection, which is unambiguously observed for the first time, is shown to lead to much more stable acceleration and higher-quality electron beams.

<sup>1</sup>Laboratoire d'Optique Appliquée, ENSTA ParisTech—CNRS UMR7639—École Polytechnique, 828 Boulevard des Maréchaux, Palaiseau 91762, France.

<sup>2</sup>CEA, DAM, DIF, Arpajon F-91297, France. \* These authors contributed equally to this work. Correspondence and requests for materials should be addressed to C.T. (email: cedric.thaury@ensta-paristech.fr).

Laser-plasma accelerators<sup>1,2</sup> have gained considerable attention for their potential in delivering, with a compact setup, quasi-monoenergetic<sup>3–5</sup>, low emittance<sup>6–8</sup>, giga-electronvolt electron beams<sup>9</sup>. The few femtosecond duration of the accelerated electrons bunches<sup>10</sup>, associated to a peak current of a few kiloamps, make these accelerators of particular interest for applications<sup>11</sup>, such as studies of electron-induced damage in biological tissues at very high dose rate<sup>12</sup>, or short wavelength, femtosecond and micrometre-source-size light beams<sup>13–19</sup>. The development of these accelerators has however been hindered by a lack of stability of the acceleration and a poor control on the electron features. These problems can be largely traced back to the injection of electrons in the plasma wake driven by the laser pulse. Electron trapping is generally achieved by the wave-breaking of the plasma wake, a process that is by nature uncontrollable and leads generally to poor-quality electrons. Controlled injection techniques, for example colliding pulse injection<sup>20</sup>, ionization-induced injection<sup>21</sup> and density-gradient injection<sup>22</sup>, have been developed to overcome this shortcoming.

These methods offer an improved control on the acceleration and lead to better electron features, but they imply generally complex setups. For this reason, self-injection remains the most common method for injecting electrons in the plasma wake. Two distinct physical mechanisms can be distinguished: longitudinal and transverse self-injection. In longitudinal self-injection, the trajectory of injected electrons is mainly longitudinal, with a negligible transverse motion. As shown by the schematic in Fig. 1a, the injected electrons pass through the laser pulse and gain energy while crossing the plasma wave. When they reach the rear of the first plasma period, their velocity exceeds the wake-phase velocity and the electrons are eventually injected. The only electrons that are trapped are those that were initially close to the axis ( $r \sim 0$ ) where the laser intensity and the wakefield amplitude are the highest and where the ponderomotive force is small. The longitudinal self-injection mechanism is analogous to one-dimensional longitudinal wave-breaking<sup>23</sup>. In contrast, transverse self-injection<sup>24</sup> is a multi-dimensional effect. It occurs in the bubble regime<sup>25–27</sup>, where the laser ponderomotive force expels electrons from the propagation axis and forms an electron-free cavity in its wake. As shown in Fig. 1b, the injected electrons are initially located at approximately one laser waist from the axis ( $r \sim w_0$ ). They circulate around the laser pulse and the bubble, and attain a velocity larger than the wake-phase velocity when reaching the axis at the rear of the bubble<sup>28–30</sup>. Except in a few papers (for example, ref. 6), trapping of quasi-monoenergetic electrons is generally attributed to transverse self-injection.

This article presents experimental and simulation results, which demonstrate that depending on laser and plasma parameters, electrons can be trapped either via longitudinal or transverse self-injection. These two types of injection are associated with energetic electrons with different properties, which allow them to be identified unambiguously. First, we show that in some conditions, electrons can be trapped successively by longitudinal followed by transverse self-injection. The experimental observation of this phenomenon was made possible by the use of a gas cell with an adjustable length. Second, we prove that trapping via longitudinal self-injection provides a stable and tunable source of energetic electrons.

## Results

**Self-injection mechanisms.** Transverse self-injection is known from three-dimensional particle-in-cell (PIC) simulations to be the most efficient trapping mechanism in the wake of an ultra-short laser pulse<sup>25,27–29</sup>. We show here that this injection can be

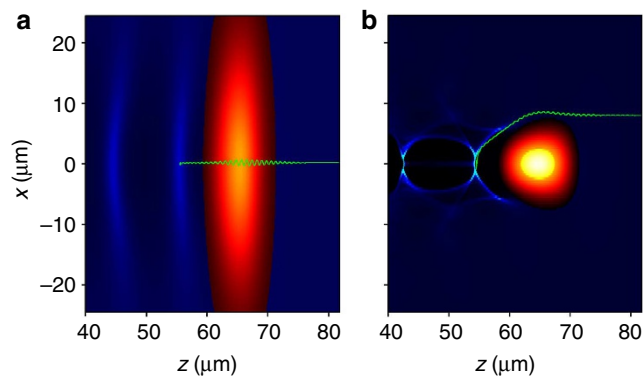


**Figure 1 | Schematic for longitudinal and transverse self-injections.** (a) Typical trajectory of an injected electron in the longitudinal self-injection mechanism. (b) Typical trajectory of an injected electron in the transverse self-injection mechanism. The blue colour scale represents the electron density. The red to yellow colour scale indicates the laser intensity. The trajectories are given by the green lines.

preceded by a noticeable trapping via longitudinal self-injection. We focus first on PIC simulations. As the aberrations on the laser beam are known to have a role on electron injection<sup>31,32</sup>, the transverse profile of laser intensity used in the simulation was taken from experimental data (Fig. 2a). The laser has an elliptical shape with some contribution of high-order modes.

Figure 2b shows the evolution of the normalized laser amplitude  $a_0$  for a 30-fs laser pulse, with an initial amplitude  $a_0 = 2$ , propagating in a plasma with density  $n_0 = 10^{19} \text{ cm}^{-3}$  (see Methods for details on the simulation). The laser pulse undergoes three cycles of focusing–defocusing because of relativistic self-focusing and self-steepening, leading to multiple injection<sup>33,34</sup>. A 2-pC bunch is injected very early in the propagation, before the first self-focusing peak, whereas a much more charged bunch (200 pC) is injected around the second self-focusing peak. A less charged bunch is injected around the third self-focusing peak.

The initial spatial distributions in the transverse plane of the electrons that are eventually injected are shown in Fig. 2c,d for the first and the second bunches, respectively. Electrons in the second bunch originate from positions close to the laser waist, as expected in the case of trapping by transverse self-injection<sup>29</sup>. In contrast, electrons in the first bunch come from regions close to the axis. When these electrons are injected, the laser spot radius is large and  $a_0$  is still low ( $a_0 \sim 2.5$ ); hence, the radial ponderomotive force close to the axis is small. Thus, on-axis electrons are only weakly deviated when crossing the laser pulse, and they remain in the region of largest accelerating field  $E_z$ . Moreover, the laser amplitude increases steeply in the region of first injection because of laser self-focusing (see Fig. 2b). This reduces the wake-phase velocity via the relativistic shift of the plasma wavelength  $\lambda_p$ <sup>35</sup>. The strongly reduced wake-phase velocity lowers the threshold for trapping, such that electrons can catch up the plasma wave and be injected despite a low  $a_0$ , similarly to density-gradient injection<sup>22</sup>.

Figure 2b shows that the conditions required to trigger longitudinal injection are fulfilled during  $\sim 40 \mu\text{m}$  only. In contrast, transverse injection occurs on  $\sim 240 \mu\text{m}$ . As a result, longitudinal injection leads to the acceleration of quasi-monoenergetic electron beams, whereas transverse injection generally results in the production of broadband electron spectra. Figure 2 also indicates that longitudinal injection takes place at the very beginning of the interaction (after  $\sim 200 \mu\text{m}$  of laser propagation), whereas transverse injection is triggered after

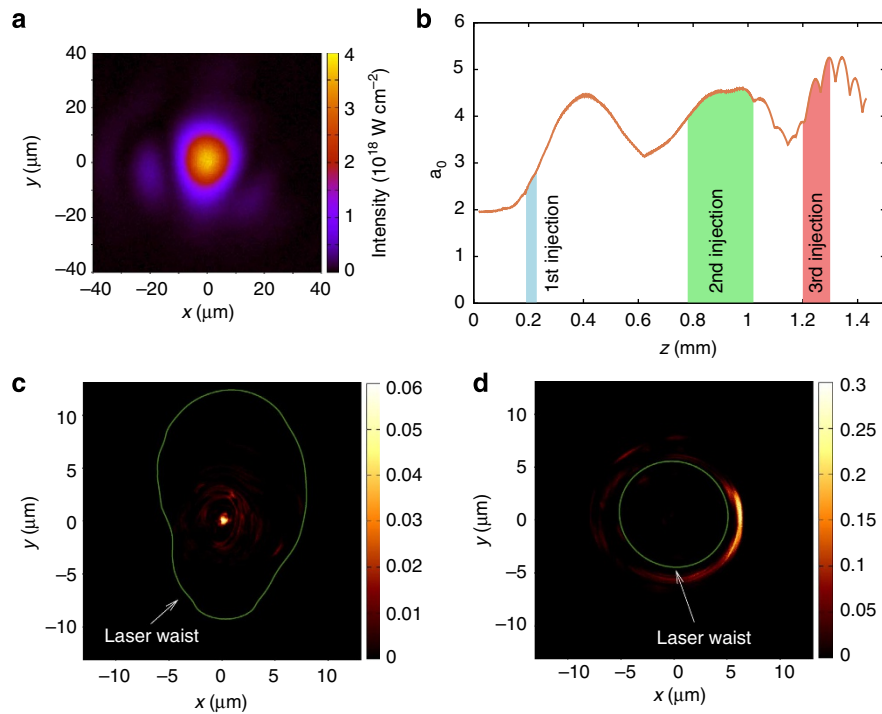


**Figure 2 | PIC simulation of the interaction.** (a) Focal spot-intensity distribution, taken from experimental data. (b) Evolution of the normalized laser amplitude. The coloured areas indicate the injection regions. (c, d) Distribution of the transverse positions from which electrons injected in the first (c) and second bunches (d) originate (the density is in arbitrary units). The  $1/e^2$  contours of the laser-pulse head are indicated in violet. The laser waist is smaller in d than in c, because of self-focusing.

significant self-focusing of the laser. As the charge in the second bunch is much larger than in the first bunch, only transverse injection is observed in experiments where the plasma length is typically in the range 2 – 10 mm.

A second feature visible in Fig. 2d is the strong asymmetry on the initial spatial distribution of electrons in the second bunch, when transverse injection models predict an even distribution around the laser waist<sup>29</sup>. This asymmetry is due to the asymmetry on the laser intensity distribution close to the waist, which breaks the cylindrical symmetry of the plasma cavity. Small changes in the focal spot lead to significant variations of the transverse distribution. Transverse injection is, hence, intrinsically unstable.

To observe experimentally sequential longitudinal and transverse injections, we used the “Salle jaune” 30 TW laser system to accelerate electrons in a gas cell, for which the length can be adjusted from 200  $\mu\text{m}$  up to 10 mm (see Methods). Typical experimental electron spectra, obtained for different cell lengths  $L$  and for an electron density  $n_e \sim 1.1 \times 10^{19} \text{ cm}^{-3}$ , are plotted in Fig. 3a. For short lengths,  $L \lesssim 1.4 \text{ mm}$ , spectra consist of quasi-monoenergetic beams with a charge in the 2–10 pC range. For  $L = 1.4 \text{ mm}$ , a second electron bunch, with a low energy, is observed. This second bunch is then accelerated to higher energy as the cell length is increased. It exhibits a broad spectrum and has a charge one order of magnitude higher than the first bunch, in the 50–100 pC range. The mean cut-off energies measured for the two electron bunches are shown in Fig. 3b. The low-charge (first) bunch reaches a maximum energy of  $\sim 250 \text{ MeV}$  for  $L \sim 1 \text{ mm}$ . Then it decreases from  $L = 1.4 \text{ mm}$ , indicating that this bunch has outrun the plasma wave and entered a dephasing region where it is decelerated by the wakefield<sup>1</sup>. In contrast, the energy of the high-charge bunch keeps increasing up to

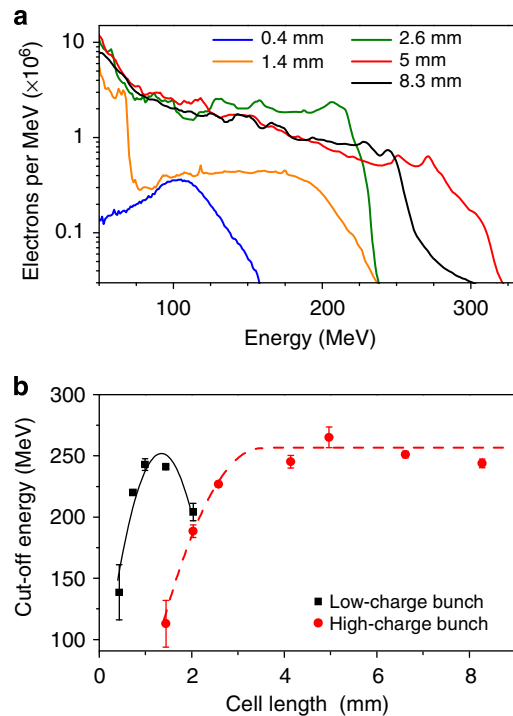


**Figure 3 | Electron spectra for  $n_e \sim 1.1 \times 10^{19} \text{ cm}^{-3}$ .** (a) Typical single-shot spectra for different cell lengths. (b) Mean 5% cut-off energy as a function of the cell length. The error bar is the s.e.m. The solid line is a parabolic fit, the dashed line is a visual guide. The peak accelerating electric field is  $E_z^{\text{max}} = 340 \pm 65 \text{ GV m}^{-1}$  for the first bunch and  $E_z^{\text{max}} = 185 \pm 40 \text{ GV m}^{-1}$  for the second bunch.

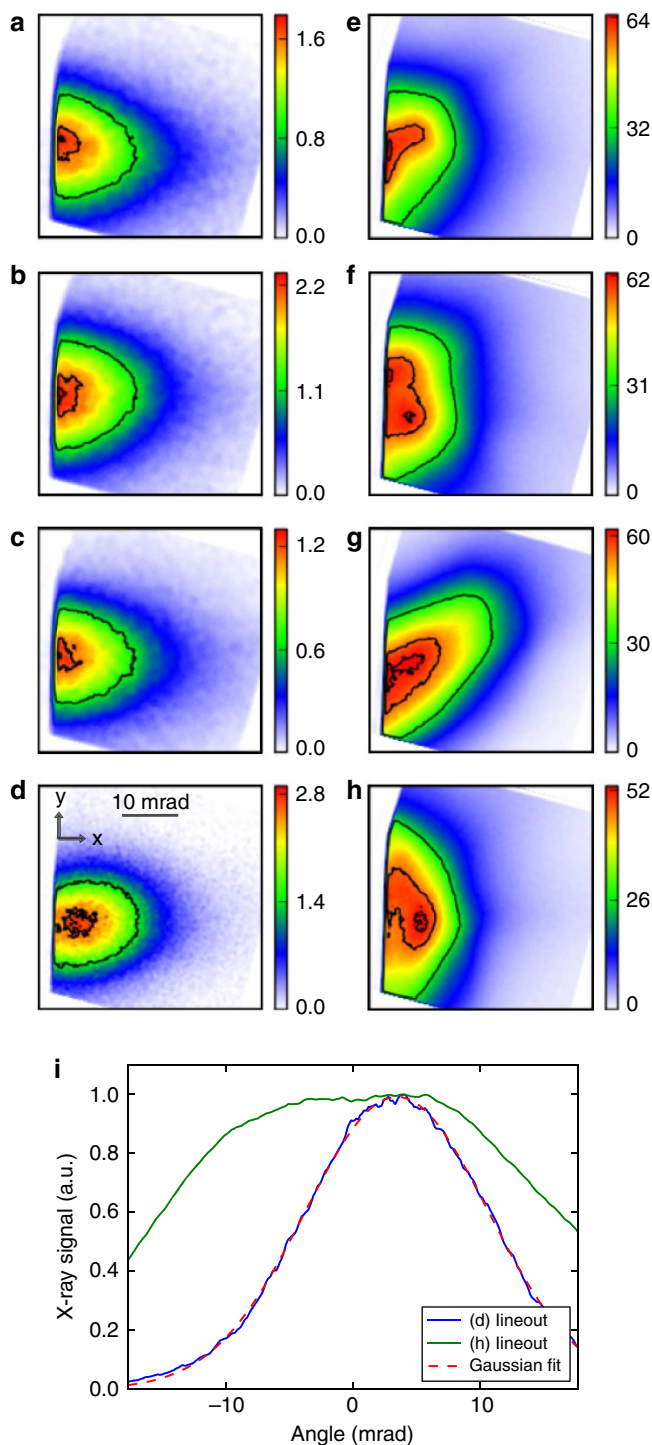


**Figure 4 | X-ray beam angular profiles for  $n_e \sim 1.1 \times 10^{19} \text{ cm}^{-3}$ .** Typical angular profiles emitted by the low-charge bunch for  $L \sim 1.2 \text{ mm}$  (**a-d**) and the high-charge bunch for  $L \sim 4 \text{ mm}$  (**e-h**). The field of view in each image is  $44 \text{ mrad} \times 44 \text{ mrad}$  and the colour scale gives the number of counts recorded by the X-ray charge-coupled device, divided by 1,000. Photon noise is reduced by a mean filter, and contour lines at 50, 90 and 98% are shown for each image. Transverse axis  $\hat{x}$  and  $\hat{y}$  are defined in **d**, where  $\hat{x}$  is the laser polarization direction. (i) Lineout in the  $\hat{y}$  direction (integrated over  $2.25 \text{ mrad}$  in the  $\hat{x}$  direction) of image **d** and **h**, and a Gaussian fit of the **d** lineout.

$\sim 270 \text{ MeV}$  for  $L = 5 \text{ mm}$ . As a result, the energy of the high-charge bunch overtakes the one of the low charge, for  $L = 2.1 \text{ mm}$ , preventing the detection of the first bunch for long plasmas.

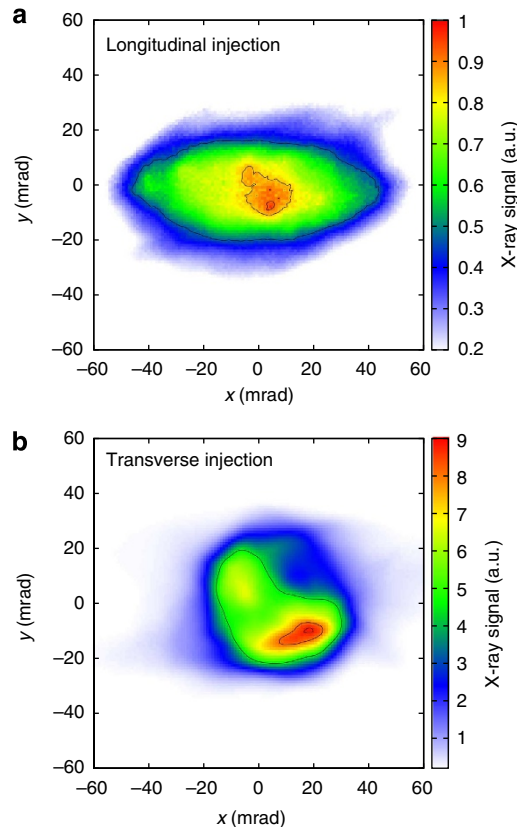


**Figure 5 | Calculated X-ray beam profiles.** The X-ray beam profiles are calculated from electron trajectories coming from PIC simulation, for the first (**a**) and the second (**b**) bunches shown in Fig. 2. Contour lines at 50, 90 and 98% are shown.

The analysis of the electron spectra clearly demonstrates the sequential injection of two electron bunches, with different charge yields and injection positions, but it does not give much insight on the injection mechanisms. More information can be obtained by analysing the betatron X-ray radiation, which arises from the transverse oscillations of accelerated electrons in the wake<sup>36,13</sup>. The angular profile of the X-ray emission depends on the electron distribution in the transverse-phase space, and as such can reveal important information on the transverse properties of the electron bunch<sup>37</sup>. X-ray beam angular profiles, presented in Fig. 4, show that the betatron radiation produced by the two bunches has very different features. The X-ray beams radiated by the high-charge bunch (Fig. 4e-h) are more intense, exhibit a lack of simple symmetry, off-centre intensity peaks, flattened transverse profiles and are constantly changing in shape. In contrast, the low-charge bunch emits very stable elliptical X-ray beams (Fig. 4a-d) with Gaussian profile and major axis along the laser polarization (see Fig. 4i). The observed difference in intensity are essentially because of the variation of the electron bunch charge.

The asymmetry and shot-to-shot fluctuations of the X-ray beam profiles radiated by the high-charge bunch suggest that its transverse distribution is also asymmetric and fluctuating, as expected for transverse injection (see Fig. 2d). To confirm that the high-charge bunch in the experiment was actually trapped by transverse self-injection, we computed the X-ray emission radiated by the first and second injected bunches in Fig. 2. The results presented in Fig. 5 show that the X-ray beam emitted by the longitudinally injected bunch (first bunch) is elliptic and Gaussian, just as the X-ray beams emitted by the low-charge

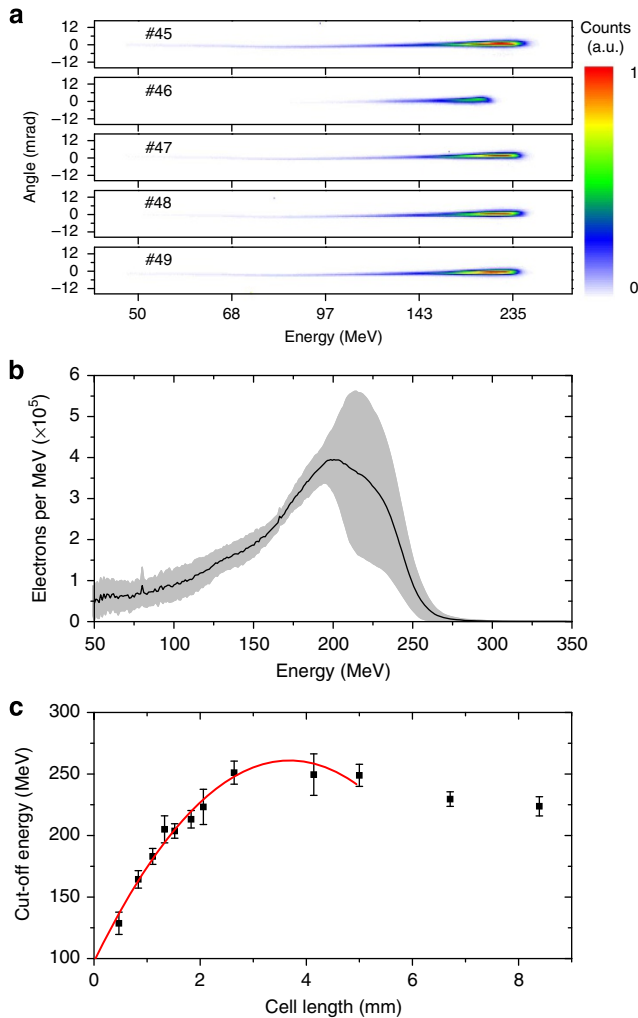


**Figure 6 | Electron spectra for  $n_e \sim 7 \times 10^{18} \text{ cm}^{-3}$ .** (a) Five consecutive raw electron spectra, for  $L = 2.7 \text{ mm}$ . (b) Mean deconvoluted spectrum. The grey area indicates the s.d. band. (c) Mean 5% cut-off energy as a function of the cell length. The error bar is the s.e.m. The parabolic fit for  $L < 5 \text{ mm}$  (red line) leads to  $E_z^{\text{max}} = 110 \pm 30 \text{ GV m}^{-1}$ .

bunch in Fig. 4a–d. The ellipse major axis is along the laser polarization in both cases. The beam profile ellipticity seems larger in simulation, suggesting that the electron bunch interacts more with the laser pulse in the simulation than in the experiment, probably because of slightly different conditions. The X-ray beam emitted by transversely injected electrons in Fig. 5b is asymmetric, presents off-centre intensity peaks and a somewhat flattened profile. These features are similar to that of the experimental profiles in Fig. 4e–h, confirming that the electrons emitting these X-ray beams were trapped by transverse self-injection.

In summary, we observed in both experiment and simulation a double injection. The first injection is due to longitudinal self-injection. It occurs very early in the laser propagation and leads to a charge of a few pC. The electron distribution is symmetric and stable shot-to-shot. The second injection is due to transverse self-injection. It occurs after significant laser self-focusing and leads to a charge of about 100 pC. The electron distribution in this case is asymmetric and changes shot-to-shot, because it depends strongly on the laser intensity profile at the injection time.

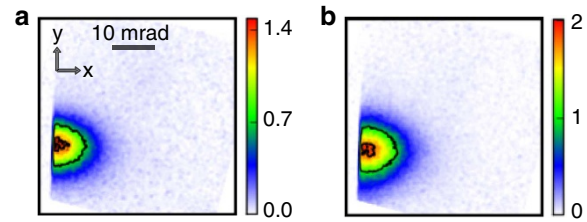


**Figure 7 | X-ray beam properties for  $n_e \sim 7 \times 10^{18} \text{ cm}^{-3}$ .** (a,b) Two typical X-ray beam angular profiles past the dephasing length (scales and image processing are identical to Fig. 4).

**A stable and tunable accelerator.** Figure 4 showed that longitudinal injection yields much more stable electron beam properties than transverse injection. These properties can be further improved by reducing the electron density. Experimental electron spectra from five consecutive shots, obtained for  $n_e \sim 7 \times 10^{18} \text{ cm}^{-3}$  and  $L = 2.7 \text{ mm}$ , are presented in Fig. 6a,b. They illustrate the good stability of the accelerator. For this density, only longitudinal injection is observed, probably because laser self-focusing is not strong enough to get transverse injection. The root-mean-square fluctuations of the peak energy are 4%, which is of the same order of magnitude as the laser amplitude fluctuations. A similar stability is observed for all cell lengths. The measured beam charge is about 5 pC for all cell lengths, with root-mean-square shot-to-shot variations of 25%. The probability of injection is 100%. The divergence of the electron beam is smaller than 2 mrad full width at half maximum (FWHM), limited by the resolution of the detector, and the energy spread is in the range 50–70 MeV FWHM.

X-ray measurements in Fig. 7 show stable and close-to-Gaussian X-ray beam profiles, confirming the longitudinal self-injection mechanism for electron trapping. Compared with  $n_e \sim 1.1 \times 10^{19} \text{ cm}^{-3}$ , observed X-ray divergences are reduced down to 10 mrad FWHM. This indicates that the electron beam has a very small transverse emittance. The latter can be estimated as follows. The Gaussian X-ray beam profile is consistent with a Maxwell–Boltzmann electron beam distribution in the transverse-phase space. In this case, the spatial variances  $\sigma_a$  with  $(a = x, y)$  and the angular variances  $\sigma'_a$  of the electron beam are linked by  $\sigma_a = \sigma'_a (2\gamma/\alpha)^{1/2} k_p^{-1}$  with  $\alpha$  the normalized amplitude of the transverse focusing force inside the plasma cavity ( $\alpha \leq 1$  with  $\alpha = 1$  for a fully evacuated cavity). The normalized transverse emittance in absence of spatial–angular correlations is  $\varepsilon_{an} = \gamma \sigma_a \sigma'_a$ . Considering that our experiment works close to full blow-out with  $\alpha \in [0.5, 1]$ , we estimate  $\varepsilon_n \in [0.57, 0.81] \pi \text{ mm mrad}$ , which is comparable to the smallest emittances measured in laser-plasma accelerators<sup>6,7,8</sup>.

Reducing the density should, in principle, increase the peak electron energy. Yet, Figs 3b and 6c show that the measured peak energy is almost the same for both densities. The accelerating fields  $E_z$  in both cases can be estimated from the parabolic fits in Figs 3b and 6c. According to Lu’s model<sup>38</sup>, the longitudinal electric field  $E_z$  should vary as  $(a_0 n_e)^{1/2}$ . Therefore, for a constant  $a_0$ ,  $E_z$  should be divided by 1.3 when  $n_e$  is divided by 1.6. In contrast, our measurements reveal that  $E_z$  is divided by 3.1. This strong decrease of  $E_z$  is the main reason for the saturation of the peak electron energy at low density. Several effects may explain the decrease of  $E_z$ . For instance, the laser intensity reached after laser pulse self-focusing and self-steepening, and the residual electron density in the plasma cavity can depend strongly on the plasma density. Departure from a perfect bubble,  $a_0$  dynamics and temporal evolution of the wakefield could also contribute to explain the large variations of  $E_z$ . In any case, the results show that the physics is more complex than suggested by simple scaling laws.

## Discussion

To improve the performance of laser-plasma accelerators and develop their applications, a precise understanding of the physics of these accelerators is mandatory, and increasing efforts have been devoted toward this goal<sup>39–42</sup>. Here we used a gas cell with an adaptable length to directly observe the injection, acceleration and dephasing of electrons. We demonstrated that electrons can be trapped either via longitudinal or transverse self-injection, and that these two types of injection lead to energetic electrons having very different features. Transverse injection is well suited for applications that require a high charge ( $\geq 100$  pC), but can cope with little stability, a large energy spread and a mediocre emittance. In contrast, longitudinal injection is ideal for applications in which a good stability and a low emittance are essential.

## Method

**PIC simulations.** Three-dimensional, fully electromagnetic PIC simulations were performed with the numerical code Calder Circ, described in ref. 43, which uses a Fourier decomposition of the electromagnetic fields in the azimuthal direction with respect to the laser-propagation direction. Seven Fourier modes ( $m = 0$  to  $m = 6$ ) were included in the simulations. The laser wavelength  $\lambda_0 = 800$  nm, the normalized laser peak amplitude  $a_0 = 2$ , the duration is 30 fs FWHM and the spatial intensity profile is taken as the projection over the modes of the experimental laser spot (shown in Fig. 2a). The mesh consists of 5,000 (in  $z$ )  $\times$  600 (in  $r$ ) cells. The cell size is  $0.096\lambda_0/2\pi$  (in  $z$ )  $\times$   $1.5\lambda_0/2\pi$  (in  $r$ ) and the time step is  $0.066\lambda_0/2\pi c$ . Positive ions are considered in the simulations as a uniform frozen background. The number of electron macroparticles per cell is 750. The longitudinal plasma profile consists of a 65  $\mu\text{m}$  long linear ramp followed by a 1.5-mm long plateau with density  $n_0 = 0.006n_c = 9.6 \times 10^{18} \text{ cm}^{-3}$ .

**Laser system.** The experiment was conducted at Laboratoire d'Optique Appliquée with the "Salle Jaune" Ti:Sa laser system, which delivers 1 J on target with a FWHM pulse duration of 35 fs and a linear polarization. The laser pulse was focused at the entrance of the gas cell with a 70-cm focal length off-axis parabola, to a FWHM focal spot size of 20  $\mu\text{m}$ . From the measured intensity distribution in the focal plane, the peak intensity was estimated to be  $4 \times 10^{18} \text{ W cm}^{-2}$ , corresponding to a normalized amplitude of  $a_0 = 1.4$ .

**Gas cell.** The target was a cell filled with neutral helium gas and whose back face can be translated continuously under vacuum, allowing to change its length in the laser-propagation direction. The front face of the cell is fixed to keep the same focal plane position with respect to the target entrance. The front and back faces had a 500- $\mu\text{m}$  diameter hole, respectively, for the entrance of the laser pulse in the gas cell and for the exit of the electron and X-ray beams. A characterization of the gas cell atomic density realized by interferometry showed a flat longitudinal density profile and yielded the calibration between backing pressure and electron density.

**Electron and X-ray beam diagnostics.** The electron spectrometer consisted of a permanent bending magnet (1.1 T over 10 cm), which deflects electrons depending on their energy, and a Lanex phosphor screen, which converts fraction of the electron energy into 546 nm light imaged by a 16 bits visible charge-coupled device camera. X-ray beams were measured with an X-ray charge-coupled device camera with 2,048  $\times$  2,048 pixels of size 13.5  $\times$  13.5  $\mu\text{m}^2$ , set at 60 cm from the gas cell and protected from the laser light by a 12  $\mu\text{m}$  Al filter.

## References

- Tajima, T. & Dawson, J. M. Laser electron accelerator. *Phys. Rev. Lett.* **43**, 267–270 (1979).
- Esarey, E., Schroeder, C. B. & Leemans, W. P. Physics of laser-driven plasma-based electron accelerators. *Rev. Mod. Phys.* **81**, 1229–1285 (2009).
- Faure, J. *et al.* A laser-plasma accelerator producing monoenergetic electron beams. *Nature (London)* **431**, 541–544 (2004).
- Geddes, C. G. R. *et al.* High-quality electron beams from a laser wakefield accelerator using plasma-channel guiding. *Nature (London)* **431**, 538–541 (2004).
- Mangles, S. P. D. *et al.* Monoenergetic beams of relativistic electrons from intense laser-plasma interactions. *Nature (London)* **431**, 535–538 (2004).
- Brunetti, E. *et al.* Low emittance, high brilliance relativistic electron beams from a laser-plasma accelerator. *Phys. Rev. Lett.* **105**, 215007 (2010).
- Plateau, G. R. *et al.* Low-emittance electron bunches from a laser-plasma accelerator measured using single-shot X-ray spectroscopy. *Phys. Rev. Lett.* **109**, 064802 (2012).
- Weingartner, R. *et al.* Ultralow emittance electron beams from a laser-wakefield accelerator. *Phys. Rev. ST Accel. Beams* **15**, 111302 (2012).
- Leemans, W. P. *et al.* GeV electron beams from a centimetre-scale accelerator. *Nat. Phys.* **2**, 696–699 (2006).
- Lundh, O. *et al.* Few femtosecond, few kiloampere electron bunch produced by a laser-plasma accelerator. *Nat. Phys.* **7**, 219–222 (2011).
- Malka, V. *et al.* Principles and applications of compact laser-plasma accelerators. *Nat. Phys.* **4**, 447–453 (2008).
- Rigaud, O. *et al.* Exploring ultrashort high-energy electron-induced damage in human carcinoma cells. *Cell Death Dis.* **1**, e73 (2010).
- Rousse, A. *et al.* Production of a keV X-ray beam from synchrotron radiation in relativistic laser-plasma interaction. *Phys. Rev. Lett.* **93**, 135005 (2004).
- Kneip, S. *et al.* Bright spatially coherent synchrotron X-rays from a table-top source. *Nat. Phys.* **6**, 980–983 (2010).
- Nakajima, K. Compact X-ray sources: Towards a table-top free-electron laser. *Nat. Phys.* **4**, 92–93 (2008).
- Schlenvoigt, H. P. *et al.* A compact synchrotron radiation source driven by a laser-plasma wakefield accelerator. *Nat. Phys.* **4**, 130–133 (2008).
- Fuchs, M. *et al.* Laser-driven soft-X-ray undulator source. *Nat. Phys.* **5**, 826–829 (2009).
- Klopper, A. Plasma screening. *Nat. Phys.* **7**, 743–743 (2011).
- Ta Phuoc, K. *et al.* All-optical Compton gamma-ray source. *Nat. Photonics* **6**, 308–311 (2012).
- Faure, J. *et al.* Controlled injection and acceleration of electrons in plasma wakefields by colliding laser pulses. *Nature (London)* **444**, 737–739 (2006).
- Pollock, B. B. *et al.* Demonstration of a narrow energy spread,  $\sim 0.5$  GeV electron beam from a two-stage laser wakefield accelerator. *Phys. Rev. Lett.* **107**, 045001 (2011).
- Gonsalves, A. J. *et al.* Tunable laser plasma accelerator based on longitudinal density tailoring. *Nat. Phys.* **7**, 862–866 (2011).
- Akhiezer, A. I. & Polovin, R. V. Theory of wave motion of an electron plasma. *Sov. Phys. JETP* **3**, 696–705 (1956).
- Bulanov, S. V., Pegoraro, F., Pukhov, A. M. & Sakharov, A. S. Transverse-wave breaking. *Phys. Rev. Lett.* **78**, 4205–4208 (1997).
- Pukhov, A. & Meyer-ter Vehn, J. Laser wake field acceleration: the highly nonlinear broken-wave regime. *Appl. Phys. B Lasers Opt.* **74**, 355–361 (2002).
- Zhidkov, A., Koga, J., Hosokai, T., Kinoshita, K. & Uesaka, M. Effects of plasma density on relativistic self-injection for electron laser wake-field acceleration. *Phys. Plasmas* **11**, 5379–5386 (2004).
- Lu, W., Huang, C., Zhou, M., Mori, W. B. & Katsouleas, T. Nonlinear theory for relativistic plasma wakefields in the blowout regime. *Phys. Rev. Lett.* **96**, 165002 (2006).
- Tsung, F. S. *et al.* Simulation of monoenergetic electron generation via laser wakefield accelerators for 5–25 TW lasers. *Phys. Plasmas* **13**, 056708 (2006).
- Kostyukov, I., Nerush, E., Pukhov, A. & Seredov, V. Electron self-injection in multidimensional relativistic-plasma wake fields. *Phys. Rev. Lett.* **103**, 175003 (2009).
- Wu, H.-C. *et al.* Electron trajectories and betatron oscillation in the wake bubble in laser-plasma interaction. *Phys. Plasmas* **16**, 073108 (2009).
- Glinec, Y. *et al.* Direct observation of betatron oscillations in a laser-plasma electron accelerator. *EPL (Europhys. Lett.)* **81**, 64001 (2008).
- Mangles, S. P. D. *et al.* Controlling the spectrum of x-rays generated in a laser-plasma accelerator by tailoring the laser wavefront. *Appl. Phys. Lett.* **95**, 181106 (2009).
- Yoshitama, H. *et al.* Physics of gases, plasmas, and electric discharges: self-injection and acceleration of monoenergetic electron beams from laser wakefield accelerators in a highly relativistic regime. *Chin. Phys. Lett.* **25**, 2938–2941 (2008).
- Oguchi, A. *et al.* Multiple self-injection in the acceleration of monoenergetic electrons by a laser wake field. *Phys. Plasmas* **15**, 043102 (2008).
- Kalmykov, S. Y. *et al.* Numerical modelling of a 10-cm-long multi-GeV laser wakefield accelerator driven by a self-guided petawatt pulse. *N. J. Phys.* **12**, 045019 (2010).
- Kiselev, S., Pukhov, A. & Kostyukov, I. X-ray generation in strongly nonlinear plasma waves. *Phys. Rev. Lett.* **93**, 135004 (2004).
- Ta Phuoc, K. *et al.* Imaging electron trajectories in a laser-wakefield cavity using betatron X-ray radiation. *Phys. Rev. Lett.* **97**, 225002 (2006).
- Lu, W. *et al.* Generating multi-GeV electron bunches using single stage laser wakefield acceleration in a 3D nonlinear regime. *Phys. Rev. ST Accel. Beams* **10**, 061301 (2007).
- Hsieh, C.-T. *et al.* Tomography of injection and acceleration of monoenergetic electrons in a laser-wakefield accelerator. *Phys. Rev. Lett.* **96**, 095001 (2006).
- Matlis, N. H. *et al.* Snapshots of laser wakefields. *Nat. Phys.* **2**, 749–753 (2006).

41. Buck, A. *et al.* Real-time observation of laser-driven electron acceleration. *Nat. Phys.* **7**, 543–548 (2011).
42. Corde, S. *et al.* Mapping the x-ray emission region in a laser-plasma accelerator. *Phys. Rev. Lett.* **107**, 215004 (2011).
43. Lifschitz, A. F. *et al.* Particle-in-Cell modelling of laser-plasma interaction using Fourier decomposition. *J. Comput. Phys.* **228**, 1803–1814 (2009).

### Acknowledgements

This work was supported by the European Research Council (PARIS ERC, contract number 226424) and EuCARD/ANAC, EC FP7 (contract number 227579). It was partly performed using high-performance computing resources of GENCI (grant number 2012-056304).

### Author contributions

S.C., C.T., G.L. and K.T.P. conceived and realized the experiment. S.C. and C.T. analysed the data. A.L. and X.D. performed the simulations. S.C., C.T., A.L., X.D., R.L. and V.M. discussed the results. S.C., C.T., A.L. and R.L. wrote the paper. G.L. and D.D. designed the gas cell. V.M. and A.R. provided overall guidance to the project.

### Additional information

**Competing financial interests:** The authors declare no competing financial interest.

**Reprints and permission** information is available online at <http://npg.nature.com/reprintsandpermissions/>

**How to cite this article:** Corde, S. *et al.* Observation of longitudinal and transverse self-injections in laser-plasma accelerators. *Nat. Commun.* **4**:1501 doi: 10.1038/ncomms2528 (2012).